Solidification paths of Al-Cu-Sn alloys: comparison of thermodynamic analyses and solidification experiments using in situ X-radiography

Sarah de Albuquerque, Guillaume Reinhart, Danielle Cristina Camilo Magalhães, José Eduardo Spinelli, Hadjer Soltani, Wafa Boumechta, Felipe Bertelli, Henri Nguyen- Thi

Solidification paths of Al-Cu-Sn alloys: comparison of thermodynamic analyses and solidification experiments using in situ X-radiography

Sarah de Albuquerque[1,2], Guillaume Reinhart[1]*, Danielle Cristina Camilo Magalhães[2,3], José Eduardo Spinelli[2,3], Hadjer Soltani[4], Wafa Boumechta[5], Felipe Bertelli[6] and Henri Nguyen-Thi[1]

[1] *Aix Marseille Univ, Université de Toulon, CNRS, IM2NP, Marseille, France*

[2] *Federal University of São Carlos, Graduate Program in Materials Science and Engineering, 13565-905 São Carlos, SP, Brazil*

[3] *Department of Materials Engineering, Federal University of São Carlos, 13565-905 São Carlos, SP, Brazil*

[4] *Badji Mokhtar University, laboratory of foundry, BP 12, 23000, Annaba, Algeria*

[5] *Badji Mokhtar University, LMGM, BP 12, 23000 Annaba, Algeria*

[6] *Sea Science Department, Federal University of São Paulo – UNIFESP, 11030-400 Santos, SP, Brazil*

* Corresponding author: guillaume.reinhart@im2np.fr

Abstract

The increasing importance of Al-Cu-Sn alloys as materials for producing self-lubricating bearing materials in automotive industries requires the development of uniform microstructures with improved performance, which could be achieved by a precise control of solidification processes. Adding Sn to Al-Cu binary alloy could dramatically alters the solidification path, generating liquid phase separation and monotectic reaction. In this paper, Al-10 wt.% Cu-X wt.% Sn (with X = 0; 5; 10 and 20) alloys have their solidification paths investigated by three different complementary approaches. Firstly, the solidification paths were calculated by using

the CALPHAD method through Thermo-Calc software revealing the sequence of transformations that could occur during the solidification of these alloys, from the formation of the initial α-Al dendrites to the final eutectic reaction. Secondly, experimental thermal analysis was carried out by DSC (Differential Scanning Calorimetry), which reveals the successive events that occur during the controlled melting and cooling of these alloys. Thirdly, directional solidification was performed on all alloys, with in situ and real-time observations achieved through the utilization of X-radiography. The comparison between the various approaches showed a suitable correspondence between the history of the alloy solidifications computed by Thermo-Calc and those obtained experimentally (DSC and directional solidification experiments). Additional information about the dynamics of each reaction was obtained during the directional solidification experiments in terms of microstructures, segregation, and the genesis of the liquid phase separation that occurred for high Sn-content alloys.

Keywords: Al-Cu-Sn alloys; Thermo-Calc; solidification microstructures; liquid phase separation; monotectic; DSC; in situ radiography

1. Introduction

Aluminium-based alloys with a miscibility gap in the liquid state such as Al-Pb, Al-Bi and Al-Sn are excellent candidates for advanced bearings in aerospace or automotive industry. As a general rule for these alloys soft metal elements such as lead, bismuth or tin could be formed as droplets distributed in harder metal matrices to produce alloys for bearing applications with very low friction coefficient and suitable wear resistance [1-8]. Although Sn has been shown to be less efficient than Pb in sliding-bearing Al alloys [9], the growing environmental concern for lead has rekindled interest in substituting appropriate soft alloying elements for such element in Al alloys.

Due to the rise in engine bearing temperatures and strains brought on by current trends in engine design, Al-Sn alloys are unable to withstand significant loads, even offering excellent antifriction capabilities. Thus, copper could be added as an alternative to hardening the Al matrix while keeping the soft Sn phase well distributed [10, 11]. Therefore, ternary Al-Cu-Sn alloys are frequently used in the manufacturing of bearing parts because these alloys combine high strength, wear resistance, and high machinability. Sn and Cu elements also contribute to the increased dimensional stability of the components. Aside from the suitable strength, Al-Cu-Sn alloys have high corrosion resistance, which is very significant for bearing applications where components may be exposed to severe conditions both in temperature and pressure [10, 11]. In a recent paper, Bertelli and co-authors [12] investigated the correlation between microstructures, tensile properties and wear resistance on directionally solidified Al-Cu-Sn alloys. They concluded that the optimal microstructure configuration for wear resistance was found to be regions with coarser α-Al dendritic phase and interdendritic regions constituted by larger Sn pockets and Al_2Cu particles [13].

In the selection of metallic alloys for tribological applications, it is mandatory to consider not only their chemical composition but also the microstructural features that occurs during the solidification process. Actually, the formation of microstructures at the solid-liquid interface (dendrites), the univariant reactions such as eutectic and monotectic, as well as the liquid phase separation in two immiscible liquids dramatically influence the final mechanical properties. As a consequence, further research into the phase transition features and solidification microstructures of ternary monotectic alloys is warranted.

The ever-increasing use of numerical simulation and modelling of the solidification processes is a very efficient way to understand or predict the microstructures formation. For instance, over the last decades, several numerical methods have been developed and applied for simulating the dendritic growth problem in its full geometrical complexity under different thermal and solutal boundary conditions and assumptions [14, 15]. However, most of such approaches did not consider the influence of gravity phenomena, such as convection in the melt and buoyancy force acting on free solid particles, which are unavoidable on Earth [16-18]. These phenomena can thus dramatically impact the solidification processes, so that the elaborated materials may strongly differ from the expected ones based only on phase diagram analyses. In particular, it is well known that fine and homogeneous dispersion of Sn or Al_2Cu particles is always difficult to achieve under conventional conditions due to the large density difference between Al liquid phase and Sn droplet or Al_2Cu particles. This disturbing gravity-induced effect is even more serious for ternary monotectic alloys that have quaternary phase equilibria comprising two immiscible liquids and two distinct solid phases. This can result in a complex variety of liquid phase separation patterns and unexpected monotectic microstructures, opening up a previously unexplored field in terms of both scientific significance and practical applications [19, 20]. One possible way to mask these gravity effects, and thus to obtain materials with desired properties, is to apply an external field during the solidification process. The effects of ultrasound on liquid

phase separation and monotectic structures of $Al_{62.6}Sn_{28.5}$ $Cu_{8.9}$ alloy were recently investigated by Zhai and co-workers [20]. The authors demonstrated that the power ultrasound is an effective and promising way to improve the solidification microstructure and mechanical properties of this alloy by preventing the spatial liquid phase separation and by reducing the macrosegregation level as ultrasound power increases.

The best technique for revealing the dynamical evolution of dendritic microstructures formation during the solidification of metal alloys is now well-established to be in situ and time-resolved X-radiography [21-24]. However, studies of immiscible alloy solidification using this powerful observation technique are hitherto very scarce. For example, Schaffer *et al.* investigated spinodal decomposition in hyper-monotectic Al-Bi and Al-Bi-Zn alloys [25] and highlighted the complex interactions between droplets. Lu *et al.* also studied liquid phase separation and the impact of bubbles on the segregation in Al-Bi alloys [26, 27]. Recently, Zhang *et al.* [28] successfully analysed the effect of solutal Marangoni force and lift force on the motion of droplets also in a hyper-monotectic Al-Bi alloy.

The current study focuses on the solidification paths of ternary Al-10 wt.% Cu-X wt.% Sn (with X = 0 wt.%, 5 wt.%, 10 wt.% and 20 wt.%) alloys. The experiments presented here used in situ X-radiography to reveal the dynamics of the solidification process, with a special emphasis on monotectic reactions and phase separations and comparing these findings with CALPHAD calculations and DSC measurements.

2. Thermo-Calc calculations based on CALPHAD method

The accurate knowledge of ternary alloy phase diagrams is a prerequisite for a better understanding of alloy behaviour aiming at focused microstructure formation during solidification. In that sense, thermodynamic calculations are an essential tool for materials

118 science and engineering and the CALPHAD (Computer Coupling of Phase Diagrams and
119 Thermochemistry) approach is now widely accepted as the most efficient strategy for
120 accelerating the development of materials. It can provide information about the phases and
121 properties of materials without or prior extensive experimental work. Consequently, this
122 approach is particularly valuable. The major goal of this Section is to determine the
123 solidification paths for the different alloys of interest, with a clear description of the successive
124 events that might be then detected experimentally either by DSC (Differential Scanning
125 Calorimetry) or during the solidification experiments.

126 The solidification paths of hypo-eutectic binary Al-Cu and Al-Sn alloys are rather standard with
127 the formation of α-Al as primary phase and then a eutectic reaction from the residual liquid.
128 However, the comprehension of the solidification paths in the ternary alloys of the Al-Cu-Sn
129 system is more complex, in part due to the occurrence of multiple transformations during the
130 cooling process [10, 11]. In a first approach, an Al-Sn pseudo-binary phase diagram with a fixed
131 amount of Cu of 10 wt.% was calculated through the CALPHAD method. For this purpose, the
132 TCAL7: Al-Alloys v7.1 database was used with the Thermo-Calc software [29] in the present
133 investigation. The pseudo-binary phase diagram considers the variation in relation to the
134 temperature of two elements (Al and Sn) while keeping the quantity of a third one (Cu) fixed,
135 being easier to read than a ternary diagram. The pseudo-binary phase diagram of the Al-10
136 wt.% Cu-X wt.% Sn system is shown in Fig.1 for Sn content varying from 0 wt.% up to 25
137 wt.%, very similar to the one given in [19]. In this composition range, two reactions are
138 detected, one monotectic at approximately 529.4°C and an eutectic at approximately 229.5°C,
139 in addition to a liquid miscibility gap that occurs when Sn content is greater than 6.6 wt.% (L"
140 represents the liquid enriched in Sn during liquid phase separation). The pseudo-binary phase
141 diagram gives a general idea of what could occur during the solidification of the ternary alloy.
142 However, the information derived from the pseudo-binary phase diagrams is not complete and

sometime could be confusing because, although useful, it is only a cross-section of a three-dimensional ternary alloy phase diagram.

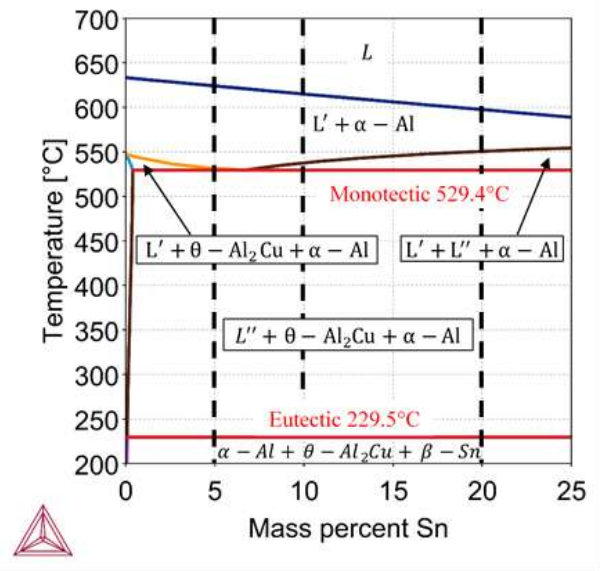

Fig.1: Al-10 wt.%Cu- X wt.%Sn pseudo-binary diagram. The three investigated compositions (5 wt.%, 10 wt.% and 20 wt.% Sn) are indicated by vertical dashed lines.

Consequently, the detailed calculation of the equilibrium solidification paths for the four alloys were performed considering the variation of all elements. It is worth mentioning that calculations using the Scheil solidification model would also provide complementary information on the solidification paths but out-of-equilibrium. However, Scheil solidification model would be less appropriate in the present case as it doesn't consider the liquid phase separation. Table 1, Table 2 and Table 3 give the respective calculated sequence of equilibrium phase transformations of the three ternary alloys. In addition, it is possible (if necessary) to determine the mass fraction of all the phases as a function of temperature, that is, the proportion in which they are formed or consumed along the solidification path. The Thermo-Calc software also provides spreadsheets that show the chemical composition of each phase depending on temperature variation, which is useful for identifying the reactions. Fig.2 depicts the

160 solidification paths for the four investigated alloys, with the successive steps during cooling
161 (from the right side to the left side) in the form of the calculated phase fraction as a function of
162 temperature.

163

164

Phase reactions	Temperature range (Thermo-Calc)	Temperature range (DSC ; Cooling)
L	Above 624°C	Above 610.5°C
L' → α-Al	From 624 to 531.5 °C	From 610.5 to 510.5 °C
L' → α-Al + θ-Al_2Cu	From 531.5 to 524.8 °C	From 510.5 to 220.5 °C
L' + α-Al → θ-Al_2Cu	From 524.8 to 229.5 °C	
L' → α-Al + θ-Al_2Cu + β-Sn	At 229.5 °C (eutectic reaction)	At 220.5 °C (eutectic reaction)

165 **Table 1** – Temperature ranges of the different reactions calculated using Thermo-Calc and
166 deduced from the temperature peaks in the DSC data during the cooling of the Al-10 wt.% Cu-
167 5 wt.% Sn alloy.

168

169

170

Phase reactions	Temperature range (Thermo-Calc)	Temperature range (DSC ; Cooling)
L	Above 615°C	Above 600.5°C
L' → α-Al	From 615 to 537.5 °C	From 600.5 to 525.5 °C
L' → α-Al + L''	From 537.5 to 529.4°C	From 525.2 to 510.5°C
L' → α-Al + L'' + θ-Al_2Cu	At 529.4 °C (monotectic reaction)	At 510.5 °C (monotectic reaction)
L'' + α-Al → θ-Al_2Cu	From 529.4 to 229.5°C	From 510.5 to 220.5°C
L'' → α-Al + θ-Al_2Cu + β-Sn	At 229.5 °C (eutectic reaction)	At 220.5 °C (eutectic reaction)

171 **Table 2** - Temperature ranges of the different reactions calculated using Thermo-Calc and
172 deduced from the temperature peaks in the DSC data during the cooling of the Al-10 wt.% Cu-
173 10 wt.% Sn alloy.

174

Phase reactions	Temperature range (Thermo-Calc)	Temperature range (DSC ; Cooling)
L	Above 597.5°C	Above 572.8°C
L' → α-Al	From 597.5 to 550.6 °C	From 572.8 to 530.3 °C
L' → α-Al + L''	From 550.6 to 529.4°C	From 530.3 to 517.8°C
L' → α-Al + L'' + θ-Al_2Cu	At 529.4 °C (monotectic reaction)	At 517.8 °C (monotectic reaction)
L'' + α-Al → θ-Al_2Cu	From 529.4 to 229.5°C	From 517.8 to 220.3°C
L'' → α-Al + θ-Al_2Cu + β-Sn	At 229.5 °C (eutectic reaction)	At 220.3 °C (eutectic reaction)

Table 3 - Temperature ranges of the different reactions calculated using Thermo-Calc and deduced from the temperature peaks in the DSC data during the cooling of the Al-10 wt.% Cu-20 wt.% Sn alloy.

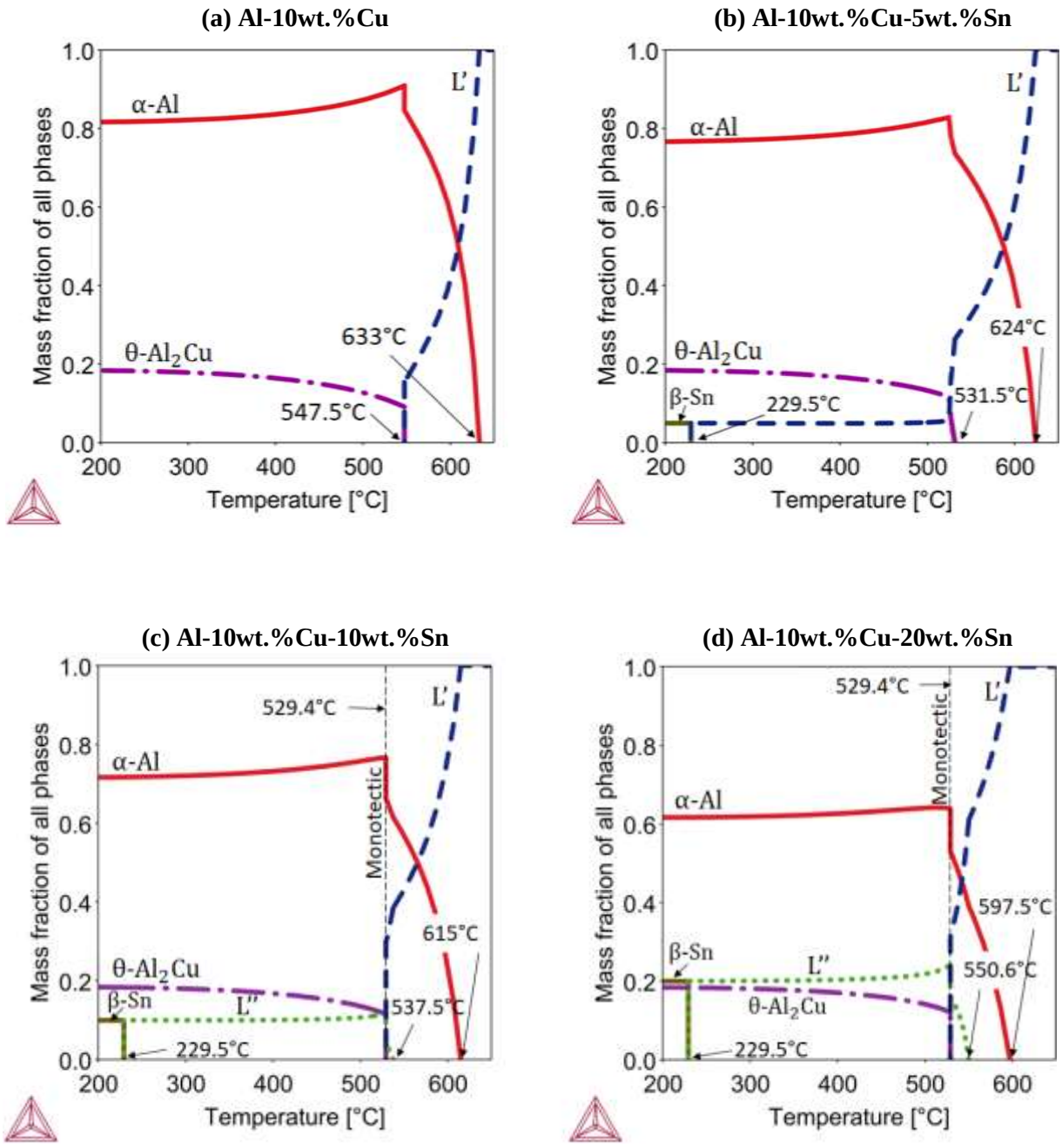

Fig.2: Equilibrium solidification paths for the four investigated alloys: a) Al-10 wt.% Cu, b) Al-10 wt.% Cu-5 wt.% Sn, c) Al-10 wt.% Cu-10 wt.% Sn, d) Al-10 wt.% Cu-20 wt.% Sn.

From the Al-Sn pseudo-binary phase diagram (Fig.1 and Fig.2a), we can see that α-Al dendrites are expected to form first at a temperature close to 633°C during the solidification of the binary Al-10 wt.% Cu alloy. Due to the solute rejection during the solidification, the liquid composition gradually increases until the formation of the eutectic phase (α-Al + θ-Al_2Cu) at 547.5°C. The Al-10 wt.% Cu alloy is a model binary alloy, that has been studied extensively in the field of solidification. For instance, the influence of a permanent magnetic field on this two-step solidification process was analysed in detail by Abou-Khalil *et al.* [30-32].

For a low addition of Sn (X = 5 wt.%), the ternary alloy Al-10 wt.% Cu-5 wt.% Sn has a similar dynamic at the beginning of its solidification path. As shown in Fig.2b and Table 1, solidification also begins with α-Al dendrites formation but at a slightly lower temperature of 624°C. Fig.2b also shows the simultaneous decrease of liquid phase L' proportion and increase of aluminium solid phase during the solidification phase down to 531.5°C. Between the temperatures 531.5°C and 524.8°C, the liquid phase L' gives birth to two solid phases (α-Al and θ-Al_2Cu) and is enriched with Cu/Sn. Between 524.8°C and $T_{eutectic}$ = 229.5°C, the liquid L' interacts with the solid α-Al to form solid θ-Al_2Cu, which explains the slow decrease from right to left of α-Al (red line) and L' (blue line), simultaneously with an increase of θ-Al_2Cu (purple dash-point line). Finally, the residual liquid L' solidifies through a eutectic reaction at $T_{eutectic}$.

For the two alloys with higher Sn compositions (X = 10 wt.% and X = 20 wt.%), solidification paths are similar to one another but more complex than for alloys with low Sn-content because of the miscibility gap in the phase diagram. As seen in Fig.2c and Fig.2d d as well as Table 2 and Table 3, additional transformations are expected during the solidification paths. Similarly, as occurred for the two low Sn-content alloys, solidification begins with α-Al dendrites formation but at different temperatures, at 615°C for the Al-10 wt.% Cu-10 wt.% Sn (Table 2)

and 597.5°C for the Al-10 wt.% Cu-20 wt.% Sn (Table 3). Fig.2c and 2d shows the simultaneous decrease of liquid phase proportion and increase of aluminium solid phase during the initial solidification phase.

In contrast to the two previous alloys, both solidification paths for Al-10 wt.% Cu-10 wt.% Sn and Al-10 wt.% Cu-20 wt.% Sn cross the liquid miscibility gap (Fig.1) during the solidification. Inside this miscibility gap, α-Al dendrites continue to grow but a liquid phase separation occurs concomitantly. A dense Sn-rich liquid L" begins to separate from L' in the form of droplets, resulting in the formation of two distinct immiscible liquids. The number and size of droplets directly depend on the initial liquid composition [33].

The liquid phase separation is clearly visible for Al-10 wt.% Cu-20 wt.% Sn in Fig.2d. For this alloy, the liquid phase separation begins at 550.6°C, with a change in the slope of the initial homogeneous liquid L' line (in blue), concomitantly with a formation of Sn-rich liquid droplet L" (in green) and a change in the slope of the α-Al line (in red). Based on Fig.2 the respective proportion and composition of the different phases could be calculated as a function of the temperature. The same liquid phase separation occurs for Al-10 wt.% Cu-10 wt.% Sn (Fig.2c) but for a very narrow range of temperature (from 537.5°C to 529.4°C), which makes it difficult to visualize in Fig.2c.

At $T_{monotectic}$ = 529.4°C, the invariant ternary monotectic reaction occurs, with the formation of two solid phases (α-Al and θ-Al_2Cu), concomitantly with the Cu/Sn-enrichment of the residual liquid phase L' due to Cu/Sn rejection during the liquid to solid phase transformation. Between $T_{monotectic}$ and $T_{eutectic}$ = 229.5°C, the residual liquid interacts with the solid α-Al to form the solid θ-Al_2Cu. This slow reaction explains the slow decrease from right to left of α-Al (red line) and L' (blue line), simultaneously with an increase of θ-Al_2Cu (purple dash-point line). The

residual liquid finally gives birth to the eutectic phase consisting of β-Sn, α-Al and θ-Al_2Cu at $T_{eutectic}$ = 229.5°C.

3. Differential Scanning Calorimetry (DSC) measurements

The differential scanning calorimetry (DSC) technique has been used to investigate the solidification paths of the different Al-Cu-Sn alloys. Calorimetric measurements are particularly convenient for monitoring the kinetics of phase transformations such as melting or solidification [34]. Changes in heat content in a solidifying material are directly proportional to the amount of solidification which has taken place and are closely related to the thermodynamic forces driving the solidification process [35]. The objective of this section is to describe the three DSC experiments that were carried out on three samples with the compositions: Al-10 wt.% Cu-X wt.% Sn (with X = 5, 10 and 20).

3.1. Experimental details

DSC measurements were carried out with a NETZCH SAT 449 F3, Jupiter differential scanning calorimeter (Selb, Germany) at School of Mines and Metallurgy Annaba (Algeria). The calorimeter was calibrated with the melting points and enthalpies of fusion (or sensibility) of high-purity elements In, Sn, Bi, Zn, Al, Ag, Au and Ni metals. In this work, three samples with the compositions: Al-10 wt.% Cu-X wt.% Sn (with X = 5, 10 and 20) were studied, cutting from ingots that were prepared at the University of Campinas (Brazil) [12]. Their chemical compositions in copper and tin were confirmed at ± 0.2 wt.% by ICP-MS (Inductively Coupled Plasma – Mass Spectrometer) at Aix-Marseille University (AGILENT 7800). Each sample of small slice in form, with approximately 20 mg ± 3 mg in weight, was placed in a sealed alumina crucible, while a second empty crucible was used as a reference. Both crucibles were inserted

into a DSC cell under a protective nitrogen atmosphere with a flow rate of 20 mL/min. The heating/cooling cycles are similar for the three experiments, at a rate of 5 K/min, in a temperature range extending from room temperature to 750°C, which is a much higher value than the melting point of the studied alloys to ensure the homogeneity of the samples. At 750°C, a holding period of 15 min was applied to homogenize the composition and liquid temperature.

3.2. DSC curves

The DSC curves obtained from the heating (melting) and the cooling (solidification) processes are presented in Fig.3 and Fig.4 respectively, for the three compositions. It is worth noticing that the heating/cooling cycles were introduced beforehand to draw a baseline or reference line with respect to nitrogen. By subtracting the baseline from the line drawn during the experiments, the transformation points presented with DSC curves will be revealed. The critical values corresponding to phase transformation temperatures on cooling are summarized in Table 1, Table 2 and Table 3.

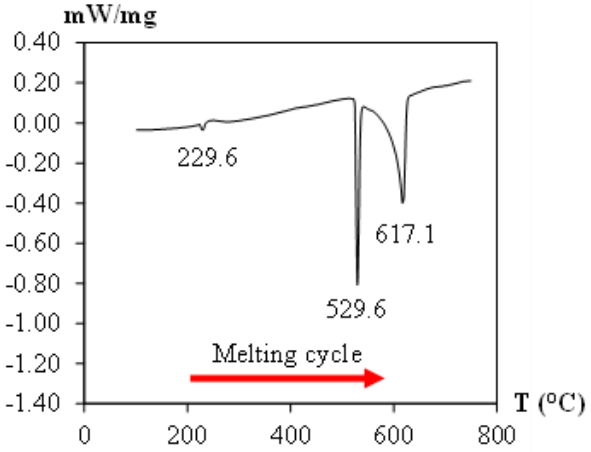

(a) Al-10 wt.% Cu-5 wt.% Sn

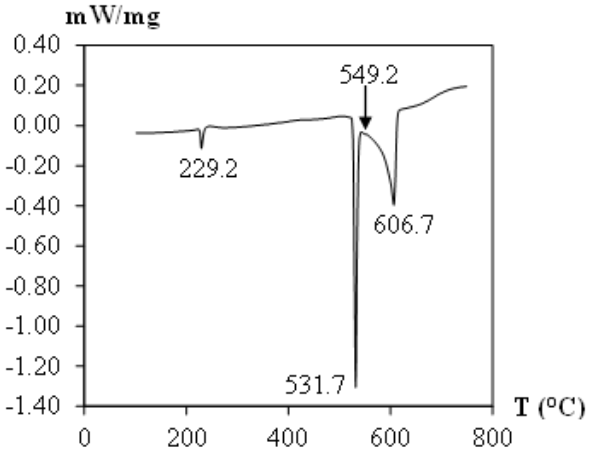

(b) Al-10 wt.% Cu-10 wt.% Sn

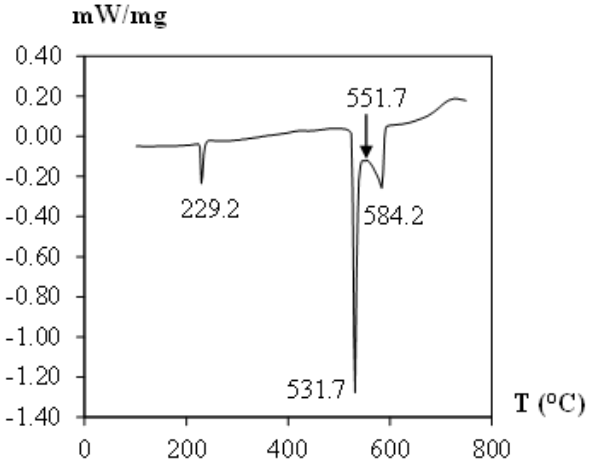

(c) Al-10 wt.% Cu-20 wt.% Sn

Fig.3: Melting DSC curves of the three different alloys recorded during sample heating, showing the endothermic peak of each transformation: (a) Al-10 wt.% Cu-5 wt.% Sn; (b) Al-10 wt.% Cu-10 wt.% Sn and (c) Al-10 wt.% Cu-20 wt.% Sn.

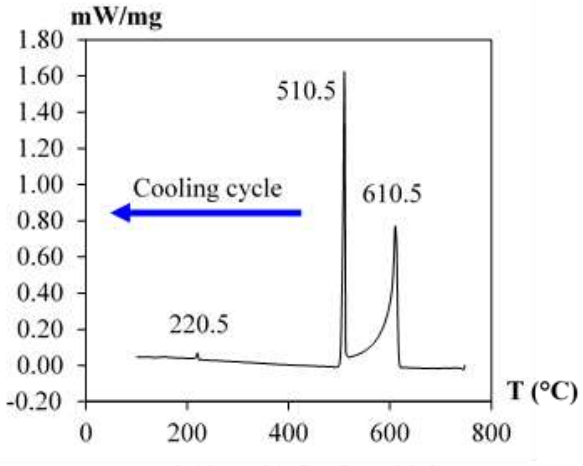

(a) Al-10 wt.% Cu-5 wt.% Sn

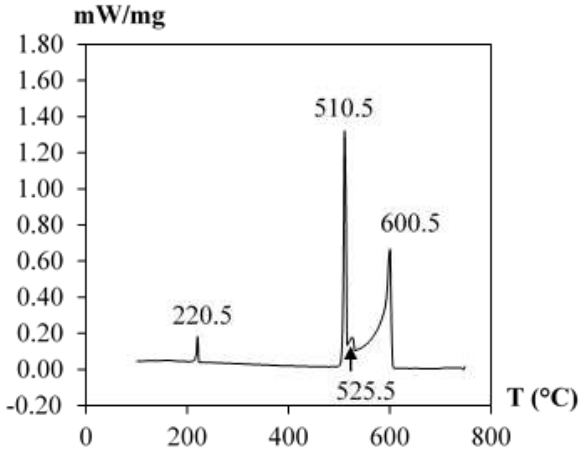

(a) Al-10 wt.% Cu-10 wt.% Sn

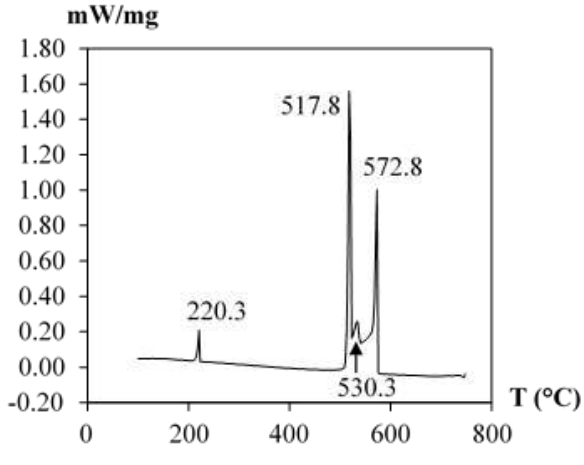

(a) Al-10 wt.% Cu-20 wt.% Sn

Fig.4: Cooling DSC curves of the three different alloys showing the exothermic peak of each transformation: (a) Al-10wt.%Cu-5wt.%Sn; (b) Al-10wt.%Cu-10wt.%Sn and (c) Al-10wt.%Cu-20wt.%Sn.

3.3. Solidification paths recorded by DSC

During the melting cycles for the three alloys (Fig.3), the curves show three clear endothermic peaks with different widths and amplitudes. For increasing temperature (from the left side to the right side of each DSC melting curves), the successive key temperatures are:

(i) $T_{eutectic}$: The first transformation corresponds to the melting of ternary eutectic β-Sn +θ-Al_2Cu + α-Al constituent. The melting temperature of the eutectic phase seems roughly identical for the three alloys, with a maximum peak slightly lower than 230°C.

(ii) $T_{monotectic}$: Secondly, a very narrow and intense peak is recorded, which corresponds to the monotectic reaction, with the melting of both θ-Al_2Cu and α-Al phases. These monotectic temperatures are almost the same for the three alloys, approximately 530°C.

(iii) By magnifying the DSC melting curves just after the sharp monotectic peak, a very shallow peak could be detected for the two high Sn-content alloys, at about 549.2°C for Al-10 wt.% Cu-10 wt.% Sn alloy and 551.7°C for Al-10 wt.% Cu-20 wt.% Sn alloy. This shallow peak is most likely the signature of the liquid phase homogenization.

(iv) $T_{\alpha\text{-Al}}$ is the temperature of the latest deep peak, which is related to the melting temperature of the α-Al dendrites. This temperature is the most sensitive to the Sn content. The larger the Sn content, the lower this temperature is.

During the cooling cycles, the number of exothermic peaks is different for the alloy with a low Sn content (Fig.4a and Table 1, Al-10 wt.% Cu–5 wt.% Sn) compared to the two alloys with larger Sn content (Fig.4b and Table 2, Al-10 wt.% Cu–10 wt.% Sn and Fig. 4c and Table 3, Al-10 wt.% Cu–20 wt.% Sn). For the two high Sn-content samples, the transformations are (from the right to the left side of the DSC curves):

(i) A first transformation at $T_{\alpha\text{-Al}}$, which corresponds to the solidification of primary α-Al dendrites. $T_{\alpha\text{-Al}}$ decreases from 610.5°C to 572.8°C when the Sn composition increases from 5 to 20 wt.%.

(ii) A small peak is visible at 525.5°C for Al-10 wt.% Cu-10 wt.% Sn alloy and at 530.3°C for Al-10 wt.% Cu-20 wt.% Sn alloy, which corresponds to the liquid phase separation, when the homogeneous liquid comes into the miscibility gap (Fig.1).

(iii) The monotectic reaction at $T_{monotectic}$ gives birth to a very narrow and intense peak, with the formation of both θ-Al_2Cu and α-Al phases.

(iv) The last transformation occurs at $T_{eutectic}$ and ends the solidification path with the formation of the eutectic phases β-Sn + θ-Al_2Cu + α-Al.

In conclusion of the DSC section, the main and unique difference between DSC cooling curves between the high Sn-content alloys (Al-10 wt.% Cu-10 wt.% Sn, and Al-10 wt.% Cu-20 wt.% Sn) and the low Sn-content alloy (Al-10 wt.% Cu-5 wt.% Sn) is a small peak that appears at a temperature between $T_{\alpha\text{-Al}}$ and $T_{monotectic}$, which most likely corresponds to the liquid phase separation, when the homogeneous liquid comes into the miscibility gap.

4. *In situ* and real time observation of Al-Cu-Sn solidification experiments

It is now well established that *in situ* and time-resolved X-radiography is a method of choice for unveiling the dynamical evolution of dendritic microstructures and grain structure formation during the solidification of metal alloys, on Earth and onboard of microgravity platforms [36]. Recently, new opportunities have arisen with the improvement of compact micro-focus sources and X-ray sensitive detectors that enable in situ and time-resolved radiography to be used in laboratory devices, with sufficient spatial and time resolutions to distinguish the microstructure

features [37, 38], enabling different orientations of the sample with respect to gravity [39] and compatible with microgravity platforms [40, 41]. Such a laboratory device was successfully used by Xavier *et al.* to analyse the morphology of the solidification interface at different cooling rates for an Al-Bi-Cu monotectic alloy [42].

4.1. Solidification experiments with *in situ* observation

In this work, directional solidification of Al-10 wt.% Cu-X wt.% Sn samples (with X = 0, 5, 10 20) were reported, using the SFINX (Solidification Furnace with IN situ X-radiography) laboratory device [37, 38]. The experimental procedure is identical to the one presented in details in [43]. The crucible-sample set was inserted inside the furnace, in direct contact with the two heaters to apply a temperature gradient along the sample. The two heating elements were controlled by two K-type thermocouples positioned 13.5 mm apart from each other. The respective temperatures of the heaters (T_{hot} and T_{cold}) were monitored independently to impose a longitudinal temperature gradient $G_{app} = (T_{hot} - T_{cold})/13.5$. For the experiments presented in this paper, solidification experiments were performed by applying a longitudinal temperature gradient G_{app} of 5.55 °C/mm. The samples were solidified by applying the same cooling rate R of 0.15 °C/s on both heaters (power-down method) and keeping constant the applied temperature gradient along the whole solidification experiment. Previous experiments have shown that these parameters lead to the formation of microstructures with features that are well distinguishable with the current imaging device. The furnace was set in horizontal position, with the main sample surface perpendicular to the gravity vector **g**. This configuration is chosen to damp gravity-related phenomena such as buoyancy [39]. The sample were prepared from the same raw ingots used for the DSC measurements, which will allow a direct comparison between the two approaches. All samples were grounded and polished to achieve dimensions of approximately 5 mm in width, 50 mm in length, and 0.20 mm in thickness.

The X-radiography system figures a micro-focus X-ray source with a molybdenum target (3 μm focal spot) providing enough photon flux and has two peaks of energy at 17.4 keV and 19.6 keV ensuring a good image contrast to study Al–based alloys [40]. In the presented experiments, a geometric magnification of approximately 5 was used for a Field-of-View (FoV) of about 5×5 mm^2 leading to an effective pixel size of approximately 4 μm. The acquisition rate was 2 frames per second. For the studied alloys, the three elements have significantly different absorption contrast so that the liquid and solid phases that are expected to form during the solidification sequence will be clearly distinguishable. The solidification sequence will be described based on the observation of the recorded images.

4.2 Image processing

Although there are significant variations in absorption contrast among the elements, certain artefacts inherent to the device make the raw images difficult to read. The artefacts result from various factors, including fluctuations in the temporal and spatial intensities of the X-ray beam or the detector background. Consequently, two different image processing were necessary, which provide complementary information about the solidification process. These image processing were done using the ImageJ software [44].

A first and commonly employed image processing technique is the *flat-field correction*, which consist in dividing the raw images (Fig.5a) by a reference image recorded just before the beginning of the solidification (Fig.5b1), when the part of the sample in the Field-of-View is almost entirely liquid [41]. The resulting image (Fig.5c1) displays a notable enhancement in readability, with an increased grey level contrast observed between the dendrites (rich in aluminium) and the liquid (enriched in copper and tin because of solute rejection during the

phase transformation). Variations in grey level in the liquid phase are related to solute composition.

A second and less known image processing, called *frame differencing*, was also applied. This technique is widely used in computer vision to highlight differences between two frames and has been successfully extended to solidification studies [45, 46]. For this purpose, the raw image of interest (Fig.5a) is divided by a raw image recorded a few seconds prior (Fig.5b2). The time interval between the two images was chosen to ensure distinct grey level contrast in the resulting images and depends on the time evolution of the solidification microstructure. In the present experiments, a value in the range of 5 to 7 seconds was chosen. This image processing was especially useful for either following the dendrite growth as depicted in Fig.5c2, where the brightest pixels reveal the solid formed during the time interval, or for detecting phase transformations for which the change in contrast is very small and was hardly distinguishable by using only the flat-field correction, such as the eutectic reaction.

In the framework of this paper, both image processing techniques were utilised to analyse the successive solidification steps during the sample cooling of the three ternary alloys.

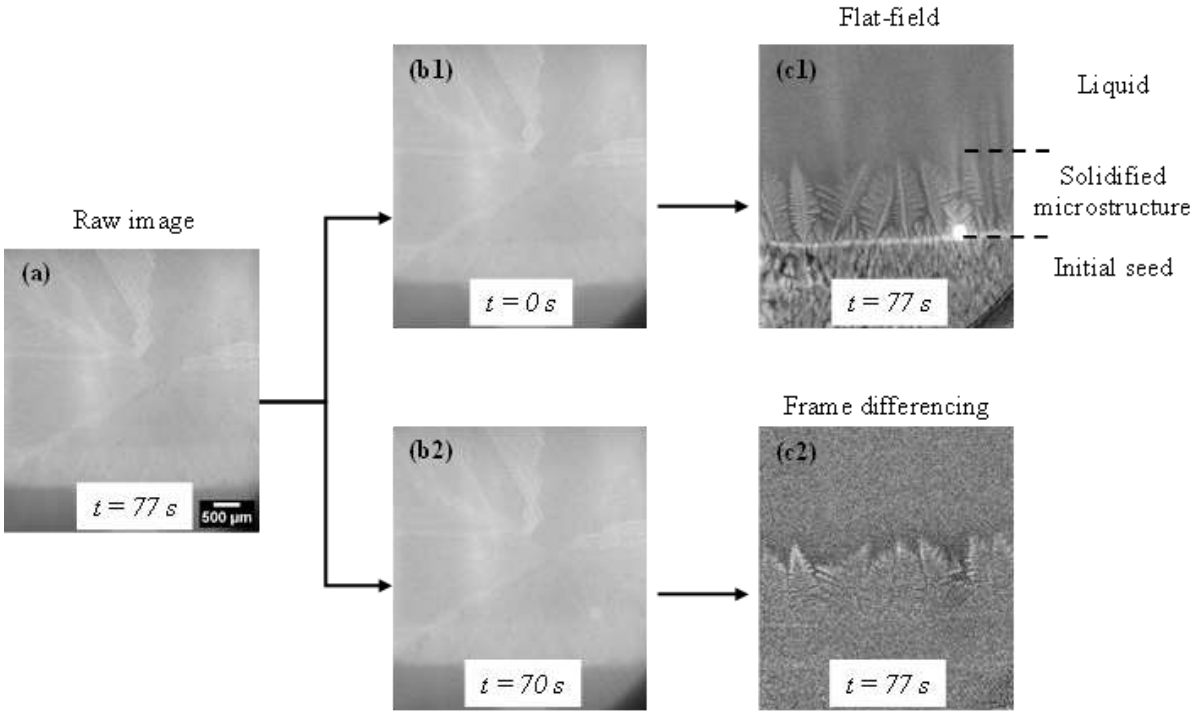

Fig.5: Illustration of the two image processing procedures used to improve the legibility of the images. (a) Raw image, (b1) reference image recorded before applying the cooling rate, (c1) result of the flat-field correction revealing more clearly the growth microstructure, (b2) raw image recorded 7 seconds before the first raw image and (c2) result of the frame differencing procedure showing the amount of solidified α-Al during the time interval.

4.3. Solidification paths observed during experiments with in situ observation

For a sake of comparison, directional solidifications of Al-10 wt.% Cu-X wt.% Sn alloys were conducted using the same cooling rate (R = -0.15 °C/s) and applied thermal gradient (G_{app} = 5.55 °C/mm). The outcomes are shown in Fig.6 for the Al-10 wt.% Cu-5 wt.% Sn alloy, in Fig.7 for Al-10 wt.% Cu-20 wt.% Sn alloy and in Fig.8 for Al-10 wt.% Cu-10 wt.% Sn alloy. Supplementary materials are provided containing videos of the solidification for all the investigated alloys. In the following figures, the displayed temperatures T_{avg} corresponds to the average value of the thermocouple temperatures used to regulate the heater elements at the time

of image capture. It will be assumed thereafter that this average temperature T_{avg} is representative of the temperature at the centre of the field of view.

a. Low tin content alloy (Al-10 wt.% Cu-5 wt.% Sn)

For the low tin content alloy, the growth of elongated α-Al grains initiates a few seconds after cooling begins, as depicted in Fig. 6a. The radiograph clearly shows dendrites in white, separated by a liquid which appears in dark grey because of copper and tin rejection during solidification. Those α-Al grains have random orientations and developed preferentially in the temperature gradient direction [37, 38]. The solidification front corresponding to the position of the dendrite tips (indicated by the dashed line) is quite flat, indicating that there is no significant transverse temperature gradient. As solidification proceeds, the entire field of view is filled with dendrites that have grown and coarsened, as depicted in Fig. 6b when the average sample temperature reaches 602°C.

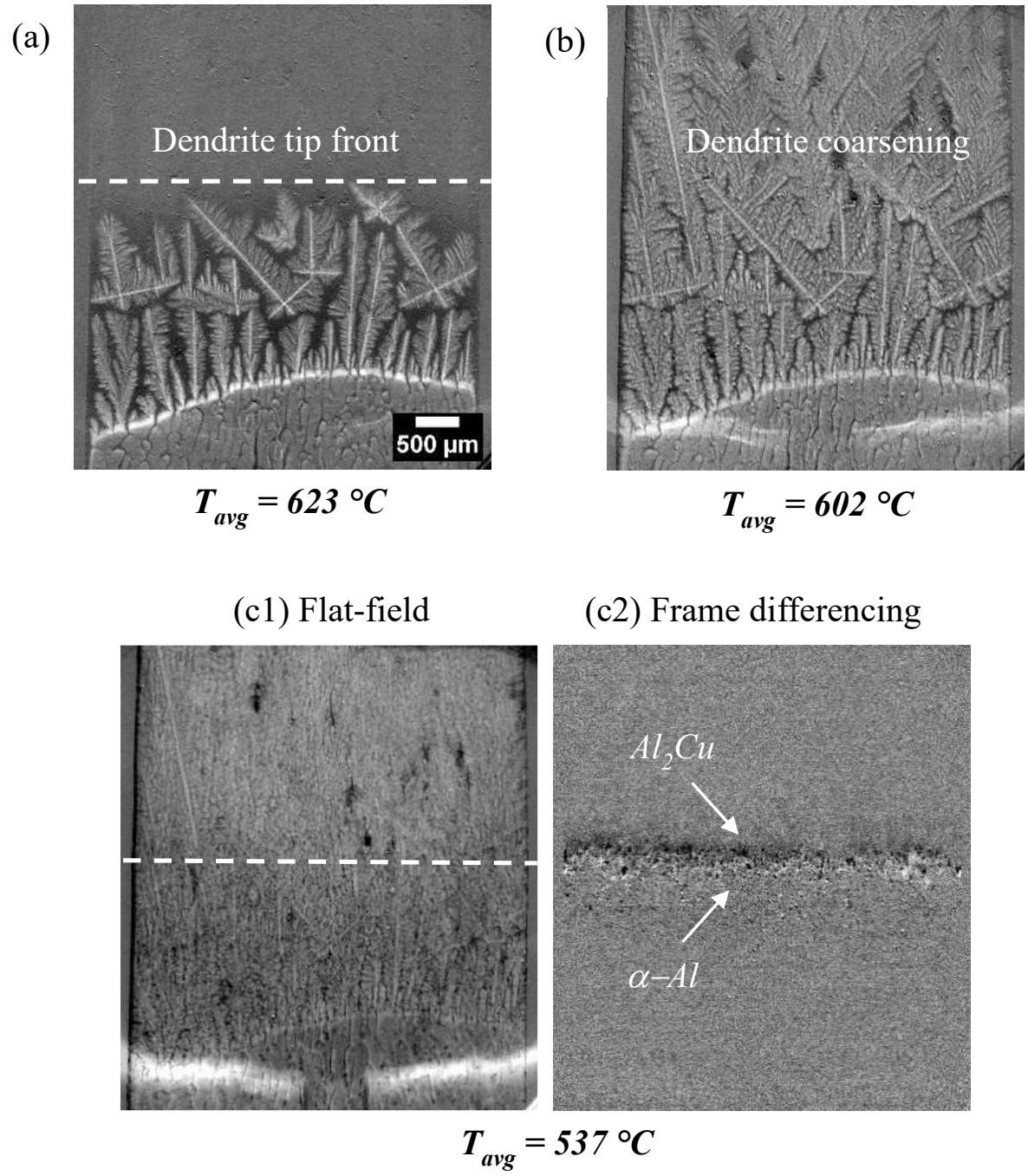

419

420 **Fig. 6**: Sequence of radiographs of Al–10 wt.% Cu–5 wt.% Sn solidification (R = -0.15 K/s and
421 G_{app} = 5.55 K/mm). Radiographs show (a) the development of columnar dendritic structures,
422 the dashed lines indicate the position of the tip of the dendrite, (b) growth and coarsening in the
423 dendrites throughout the field of view, and (c) the reaction L' → α-Al + θ-Al_2Cu. Left-hand
424 side: flat-field image. Right-hand side: image with frame differencing correction highlighting
425 the formation of Al_2Cu and α-Al.

Fig.6c shows observations made at a much lower temperature of 537°C by applying flat-field correction (Fig.6c1) and frame differencing (Fig.6c2) to the same radiograph. In Fig.6c1, the dendritic network has experienced a long coarsening period, and the secondary and ternary arms are now difficult to distinguish. In addition, the half-top part of the sample is brighter than the half-bottom part of the sample. This change in grey level is abrupt as indicated by the dashed line, which means that a phase transformation occurs at a given temperature. Fig. 6c2 (frame differencing image) reveals the formation of a dark layer above a white layer at this given temperature. The white layer can be attributed to the formation of the α-Al phase, which is less absorbing, and the dark layer can be attributed to the formation of the Al_2Cu phase, as it is more absorbing than the initial liquid phase. Accordingly, Al_2Cu formation is probably the cause of the darkening seen in the lower part of Fig. 6c1. The formation of these phases at this temperature would be in line with the theoretical solidification path (Fig.2 and Table 1).

b. Medium and high tin content alloys (Al-10 wt.% Cu-10 wt.% Sn and Al-10 wt.% Cu-20 wt.% Sn)

For the two alloys with higher Sn compositions (X = 10 wt.% and X = 20 wt.%), the expected reactions following the formation of the primary α-Al phase are *(i)* the liquid phase separation and *(ii)* a monotectic reaction. Similar observations have been made for the two alloy compositions and therefore the following section will focus first on the solidification of Al-10 wt.% Cu-20 wt.% Sn for which the phenomena were observed more clearly.

As for the low tin content alloy, the first stages of solidification consist of the formation of elongated grains with random orientations and developing in the temperature gradient direction (Fig. 7a and Fig. 7b), followed by a coarsening period. Fig.7c shows observations made at a

lower temperature of 543°C by applying flat-field correction (Fig.7c1) and frame differencing (Fig.7c2) to the same radiograph. This time, three regions with different contrasts indicated by dashed lines can be distinguished in Fig. 7c1: the top part and bottom parts of the image are brighter than the middle part. Fig. 7c2 (frame differencing image) reveals, from top to bottom, a light grey layer containing small black dots above a dark layer, and a white region also containing small black dots. The light grey layer can be attributed to the depletion in Sn of the L' liquid due to the formation of the Sn-rich L'' liquid, appearing as small black droplets. The black layer corresponds to the sudden formation of a large amount of the Sn-rich liquid L'' during the liquid phase separation and is the cause of the darkening seen in the middle part of Fig.7 c1. Finally, the white region agrees with the formation of a high amount of α-Al as expected during the monotectic reaction and is the cause of the brightening seen in the bottom part of Fig.7 c1. It is worth mentioning that in the latter case the black dots in the white layer can be either Al_2Cu or L" phases that are both absorbing and thus couldn't be distinguished with the current spatial resolution. This sequence of phase formation would only partly be in line with the theoretical solidification path (Fig.2 and Table 1), as the phase separation leading to the formation of the Sn-rich liquid L'' didn't occur with a linear increase of the mass fraction of L'' but in two steps: firstly, the progressive formation of small droplets and secondly the sudden occurrence of a large amount of L'' as indicated in Fig.7 c2.

For a sake of completeness, the image sequence for the Al–10 wt.% Cu– 10 wt.% Sn alloy is displayed in Fig.8. The same steps are visible: formation of elongated grain (Fig.8a), coarsening (Fig.8b), phase separation and monotectic reaction (Fig.8c). It is worth noting that the light grey layer wasn't detected in Fig.8c, most probably because the phase separation and the monotectic reaction occurred at closer temperatures and the change in composition of L' was lower.

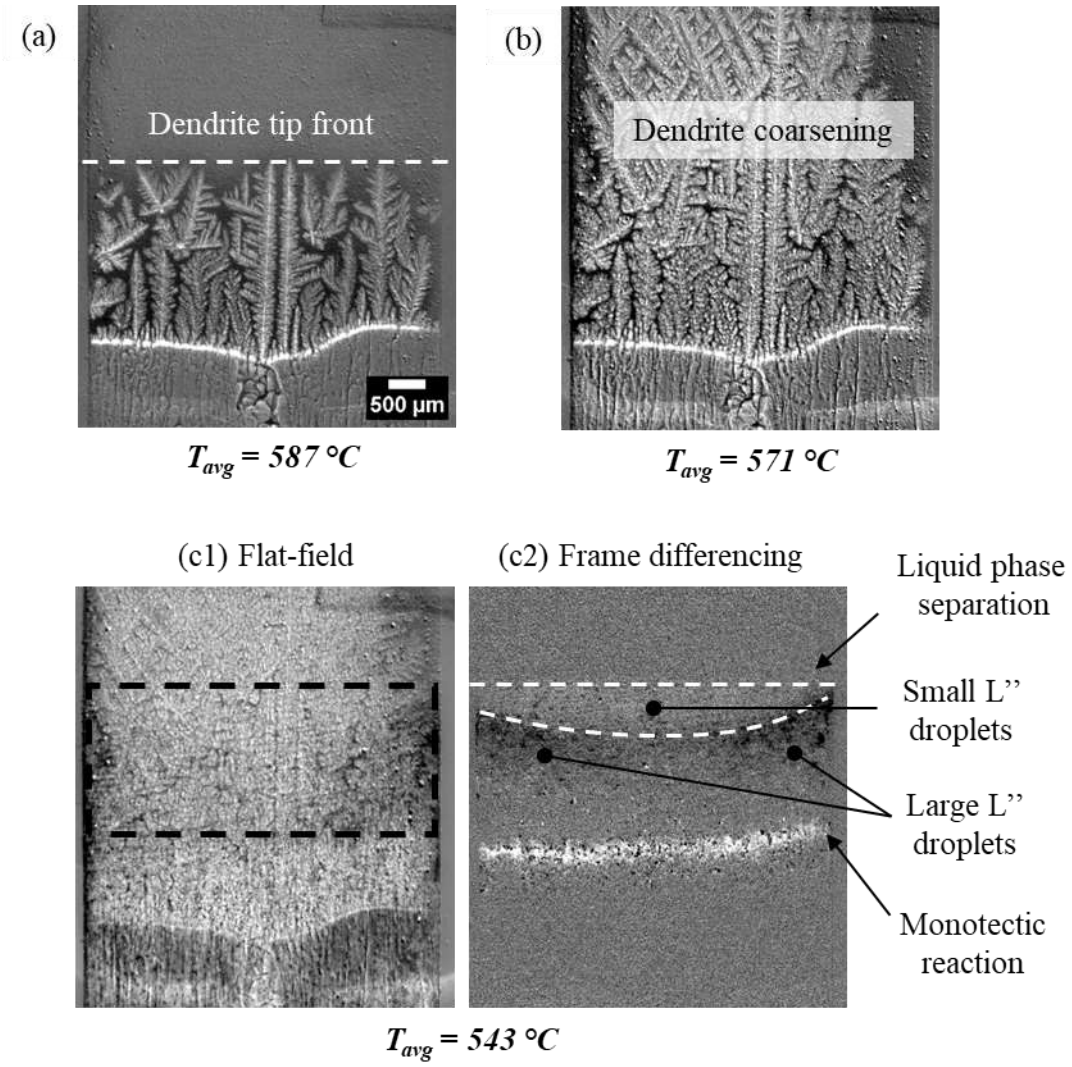

473

474 **Fig. 7**: Sequence of radiographs of Al–10 wt.% Cu– 20 wt.% Sn solidification (R = -0.15 K/s
475 and G_{app} = 5.55 K/mm). Radiographs show (a) the development of columnar dendritic
476 structures, the dashed lines indicate the position of the tip of the dendrite, (b) growth and
477 coarsening in the dendrites throughout the field of vision, and (c) the liquid phase separation
478 and monotectic reaction. On the left-hand side: flat-field image with the separation of the liquid
479 phase highlighted in the frame. On the right-hand side: image with frame differencing
480 correction, highlighting the liquid phase separation (L'+L") and the monotectic reaction.

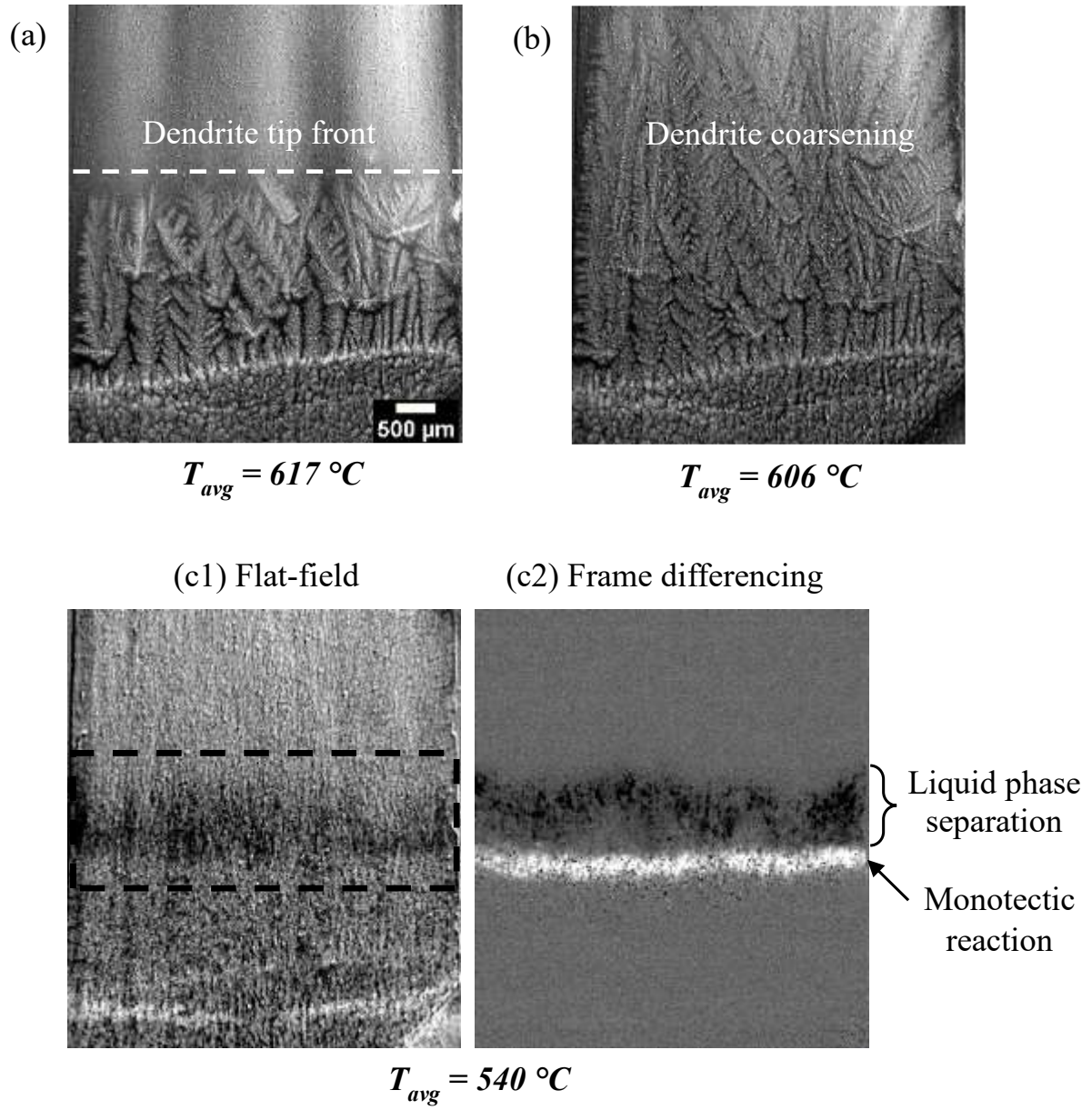

481

482 **Fig. 8**: Sequence of radiographs of Al–10 wt.% Cu– 10 wt.% Sn solidification (R = -0.15 K/s
483 and G_{app} = 5.55 K/mm). Radiographs show (a) the development of columnar dendritic
484 structures, the dashed lines indicate the position of the tip of the dendrite, (b) growth and
485 coarsening in the dendrites throughout the field of vision, and (c) the liquid phase separation
486 and monotectic reaction. On the left-hand side: flat-field image with the separation of the liquid
487 phase highlighted in the frame. On the right-hand side: image with frame differencing
488 correction, highlighting the liquid phase separation (L") and the monotectic reaction.

5. Discussion

In summary, the solidification paths of Al-10 wt.% Cu-X wt.% Sn (with X = 0; 5; 10 and 20) alloys were successfully investigated by using three different and complementary approaches, namely Thermo-Calc calculations, DSC thermal analysis and solidification experiments with *in situ* X-radiography monitoring. All these approaches clearly establish that the addition of tin element in alloys dramatically alters the solidification behaviour and associated microstructure, that could generate liquid phase separation and monotectic reaction. Since these alloys are multi-element alloy systems, theoretical understanding of the successive steps during the solidification phase is rather difficult, due to the metallurgical complexity. Qualitatively, the three analysis methods show an excellent agreement for the successive steps that are observed during the solidification but large discrepancies are found for the temperatures of reactions.

For the three ternary alloys considered in this study, Al-10 wt.% Cu-X wt.% Sn (with X = 5; 10 and 20), the first solid consists of elongated α-Al grains, more or less oriented along the imposed temperature gradient as expected. The only difference between the three alloys is the temperature $T_{\alpha\text{-}Al}$ at which dendrites are expected to form. According to the phase diagram, the higher the Sn composition is, the lower $T_{\alpha\text{-}Al}$. Thermo-calc calculations give decreasing values from 624°C to 597.5°C, while DSC measurements during cooling show peaks starting at values that decrease from 610°C to 572.8°C when the Sn composition increases from 5 to 20 wt.%. From solidification experiments with in situ observation, $T_{\alpha\text{-}Al}$ values can be estimated from 623°C to 587°C. The discrepancies between all those values are within the range of uncertainty of each method. Indeed, Thermo-Calc values are calculated at equilibrium based on phase diagram, whereas *(i)* the DSC curves are measured during sample melting/cooling, slightly out of equilibrium, which requires careful control of melting/cooling rates and volume fractions of the disperse phase to obtain accurate results, and *(ii)* estimates from solidification experiments

514 are limited by the approximate knowledge of temperature distribution along the sample in the
515 Field-of-View.

516 For the low tin content alloy, Thermo-Calc calculations predict a second phase transformation,
517 in a very narrow range of temperature, between 531.5°C and 524.8°C (see Table 1). This phase
518 transformation appears as a sharp peak in DSC cooling curve at a much lower temperature of
519 510.5°C (Fig.4 and Table 1) and has also been revealed during solidification experiment at a
520 mean temperature of 537°C. For this phase transformation, solidification experiment and
521 Thermo-Calc calculations are in good agreement, whereas temperature value from DSC
522 analysis seems too low. A third and final phase transformation is the eutectic reaction, which
523 occurs at about 230°C according to Thermo-Calc calculations, 220.5°C from both DSC cooling
524 curve and solidification experiment. Like for the temperature $T_{\alpha\text{-}Al}$ at which dendrites are
525 expected to form, those discrepancies are most likely due to uncertainty inherent to each
526 method.

527 For the two alloys with higher Sn compositions (X = 10 wt.% and X = 20 wt.%), the expected
528 reactions following the formation of the primary α-Al phase are *(i)* the liquid phase separation
529 followed by *(ii)* a monotectic reaction and a final transformation by *(iii)* the eutectic reaction.
530 Those observations have been indeed made for the two alloy compositions whatever the
531 approach is. The liquid phase separation is predicted at 537.5°C and 550.6°C for Al-10 wt.%
532 Cu-10 wt.% Sn and Al-10 wt.% Cu-20 wt.% Sn respectively by Thermo-Calc software (Table
533 2 and Table 3). Values obtained by DSC measurements during cooling are significantly lower,
534 at 510.5°C and 517.8°C for the two alloys (Fig. 4, Table 2 and Table 3), but only slightly lower
535 at 533°C and 540°C by DSC measurements during melting (Figure 3). Directional solidification
536 experiments give roughly the same value of 540°C for both alloys. For the directional
537 solidification experiments, these very approximate values are most likely due to the uncertainty
538 about the temperature distribution in the Field-of-View, as well as the limited spatial resolution

539 which prevents the determination of an accurate value for the first Sn droplet nucleation. Nor
540 should we rule out the possibility of convection or buoyancy effects on Sn droplets at this stage
541 [25, 47]. The subsequent reaction is the monotectic reaction, that is scheduled by Thermo-Calc
542 calculations at a plateau of 529.4°C for both alloy compositions. The peaks obtained by DSC
543 measurements during cooling start at 510.8°C and 517.8°C for Al-10 wt.% Cu-10 wt.% Sn and
544 Al-10 wt.% Cu-20 wt.% Sn respectively, but 525.5 and 522.8°C by DSC measurements during
545 melting, which better agrees with the Thermo-Calc calculated value of 529.4°C.

546 As previously mentioned, the approximate value of the temperature for the directional
547 solidification experiments makes it hard to compare with Thermo-Calc calculations and DSC
548 measurements. However, it is possible to estimate the temperature difference ΔT between the
549 beginning of the phase separation and the monotectic reaction based on their respective position
550 in the field of view in the radiographs (Fig.9).

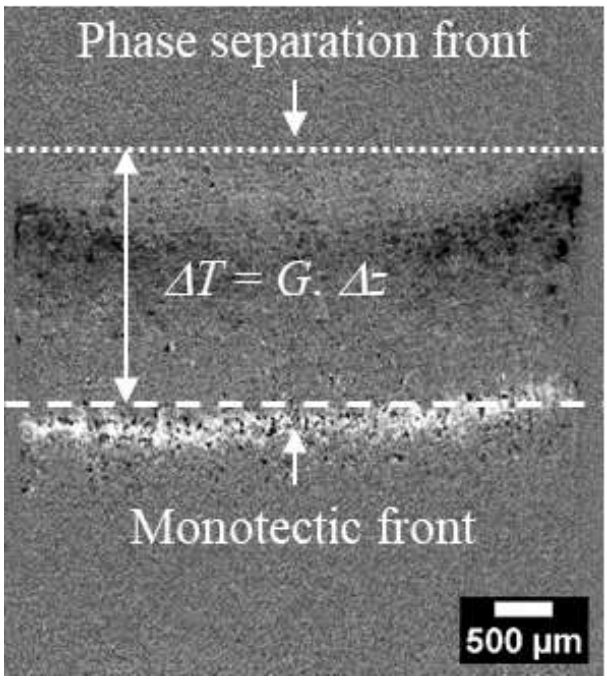

551

552 **Fig. 9**: Determination of the temperature difference between the beginning of the phase
553 separation (dotted line) and the monotectic reaction (dashed line). (Al–20 wt.% Cu– 10 wt.%
554 Sn, R = 0.15 K/s and G_{app} = 5.55 K/mm).

555

556 It has been previously shown in [37] that the actual temperature gradient in the sample G_{sample}
557 can be estimated by measuring the propagation velocity of the solidification front V_{front} and then
558 using the relation $G_{sample} = R/V_{interface}$ with R the applied cooling rate. Here, the propagation of
559 the monotectic front was used for both alloys to determine G_{sample}. The temperature difference
560 between the phase separation and the monotectic reaction is then $\Delta T = G_{sample}.\ \Delta z$, with Δz the
561 distance between the beginning of the phase separation and the monotectic front. A temperature
562 difference of 4°C is obtained for the Al-10 wt.% Cu-10 wt.% Sn alloy, and a temperature
563 difference of 11°C is obtained for the Al-10 wt.% Cu-20 wt.% Sn alloys. From Thermo-Calc
564 calculation a temperature difference of 8.1°C is predicted for the Al-10 wt.% Cu-10 wt.% Sn
565 alloy and a temperature difference of 21.2°C is predicted for the Al-10 wt.% Cu-20 wt.% Sn
566 alloys. The impact of Sn content on the temperature difference qualitatively agrees between the
567 measured and the predicted values.

568 Those discrepancies can be attributed to various factors, such as the fact that Thermo-Calc
569 calculations don't consider the impact of nucleation and growth undercoolings. It is indeed
570 well-known in directional solidification that the temperature of dendrite tips is lower than the
571 equilibrium temperature due to solute rejection leading to the occurrence of constitutional
572 undercooling [48]. The same remark applies to the monotectic and eutectic solidification fronts.
573 Droplet formation also occurs at a different temperature than the phase separation equilibrium
574 temperature as they most probably appear on the sample wall by heterogeneous nucleation.
575 Another factor is that the composition of the sample could have changed in the field of view
576 due to segregation occurring during the stabilisation and solidification steps. The temperature
577 difference wasn't estimated from the DSC measurements as it wasn't possible to accurately
578 determine the beginning of the phase separation and monotectic reaction due to the
579 superimposition of their respective peaks in the curves.

Ultimately, the final eutectic phase transformation, which is predicted at about 230°C in Thermo-Calc calculations, is observed at 223°C from both DSC cooling curve and solidification experiment, which is in good agreement.

6. Conclusions

Determination of reliable solidification paths for ternary alloys is difficult. In the literature, several different approaches are used that give sometime diverging results and subject to large uncertainties. In this paper, the solidification paths of Al-10 wt.% Cu-X wt.% Sn (with X = 0; 5; 10 and 20) alloys were successfully investigated by using three different and complementary approaches, namely Thermo-Calc calculations, thermal analysis and solidification experiments with in situ X-radiography monitoring. This paper provides a comparison between those methods, both qualitatively (nature of the successive phase transformations) and quantitatively (temperature at which each phase transformation occurs).

The main qualitative conclusion is that all these methods describe correctly the successive phase transformations, from the initial α-Al dendrite growth to the final eutectic transformation of the residual liquid. Depending on the alloy composition, the liquid phase separation and the monotectic reactions are successfully predicted by Thermo-Calc calculations and experimentally detected during DSC measurements or solidification experiments with in situ observation. It should be emphasized that in situ observation revealed some unexplained features that occur during the liquid phase separation. It would be easy to justify these phenomena by convection and/or buoyancy effects associated to gravity but further studies are required to clearly determine their origins.

Evaluation of the temperature at which each phase transformation occurs has been also carried out by the different methods. A wide dispersion has been found, up to 10°C for some phase

transformations. Thermo-Calc calculations and thermodynamic measurements have intrinsic limitations. For solidification experiment, the main weakness is the accurate knowledge of the temperature distribution in the Field-of-View. Further improvements of the current apparatus are required to achieve the necessary temperature resolution. It is also worth mentioning that investigations focused on the effect of Sn addition and of the various solidification parameters on the growth of α-Al dendrites and Sn droplet size and spatial distribution could be performed based on the X-radiography images. Unfortunately, analyses of the X-ray images to determine phase fractions, as performed in other studies [49-51] was not possible. This is due to the use of a polychromatic laboratory source in this study, which prevents a straightforward phase fraction extraction. Additionally, significant coarsening of the phases during cooling may hinder direct comparison of the 3D reconstructions and radiographs, as successfully carried out by Chao *et al.* [49]. Such investigations will be the topic of future complementary studies.

Acknowledgments

This research work is supported by the French National Space Agency (CNES) n°200761/00. Mrs Sarah De Albuquerque benefits a PhD grant from the French Embassy in Brazil. Pr. Amauri Garcia and Pr. Noé Cheung are also acknowledged for their help to the first analyses and ingot preparation. This study was financed in part by the Coordenação de Aperfeiçoamento de Pessoal de Nível Superior—Brasil (CAPES)—Finance Code 001.

Appendix A. Supplementary data

Supplementary data related to this article can be found at (link to supplementary material)

References

[1] X.F. Wu, G.A. Zhang, F.-F. Wu, Effect of Sn addition and heat treatment on microstructure and wear resistance of hypereutectic Al-Si-Cu-Mg alloy, Cailiao Rechuli Xuebao/Transactions of Materials and Heat Treatment, 33 (2012) 85-90.

[2] G. Ran, J.-E. Zhou, S. Xi, P. Li, Microstructure and morphology of Al–Pb bearing alloy synthesized by mechanical alloying and hot extrusion, Journal of Alloys and Compounds, 419 (2006) 66-70.

[3] X. Wu, G.A. Zhang, Influence of Sn Content on the Microstructure and Dry Sliding Wear Behaviour of Hypereutectic Al-20Si Alloy, Advanced Materials Research, 299-300 (2011) 265-268.

[4] Z.C. Lu, M.Q. Zeng, Y. Gao, M. Zhu, Significant improvement of wear properties by creating micro/nano dual-scale structure in Al-Sn alloys, Wear, 296 (2012) 469-478.

[5] F. El-Salam, A. El-Khalek, R. Nada, L. Wahab, H. Zahran, Effect of Sn content on the structural and mechanical properties of Al–Si alloy, Mater. Sci. Eng. A-Struct. Mater. Prop. Microstruct. Process., 527 (2010) 1223-1229.

[6] X. Liu, M.Q. Zeng, Y. Ma, M. Zhu, Promoting the high load-carrying capability of Al–20 wt%Sn bearing alloys through creating nanocomposite structure by mechanical alloying, Wear, s 294–295 (2012) 387–394.

[7] Q. Yang, Z.P. Sun, Z.M. Wang, Effects of Sn, Si, and Cu addition on the microstructure and properties of hypermonotectic Al92Bi8 alloy, Mater. Sci. Eng. A-Struct. Mater. Prop. Microstruct. Process., 756 (2019) 71-81.

[8] N.I. Noskova, N.F. Vil'danova, Y.I. Filippov, R.V. Churbaev, I.A. Pereturina, L.G. Korshunov, A.V. Korznikov, Preparation, deformation, and failure of functional Al-Sn and Al-Sn-Pb nanocrystalline alloys, Phys. Metals Metallogr., 102 (2006) 646-651.

[9] R. Mittal, A. Tomar, D. Singh, Wear Behavior of Disk Shape Spray Formed Al-Si-Pb Alloys, Journal of Materials Engineering and Performance, 23 (2014) 975-981.

[10] H.R. Kotadia, A. Das, E. Doernberg, R. Schmid-Fetzer, A comparative study of ternary Al-Sn-Cu immiscible alloys prepared by conventional casting and casting under high-intensity ultrasonic irradiation, Mater. Chem. Phys., 131 (2011) 241-249.

[11] H.R. Kotadia, E. Doernberg, J.B. Patel, Z. Fan, R. Schmid-Fetzer, Solidification of Al-Sn-Cu Based Immiscible Alloys under Intense Shearing, Metall. Mater. Trans. A-Phys. Metall. Mater. Sci., 40A (2009) 2202-2211.

[12] F. Bertelli, C. Brito, I.L. Ferreira, G. Reinhart, H. Nguyen-Thi, N. Mangelinck-Noel, N. Cheung, A. Garcia, Cooling thermal parameters, microstructure, segregation and hardness in directionally solidified Al-Sn-(Si;Cu) alloys, Materials & Design, 72 (2015) 31-42.

[13] F. Bertelli, E.S. Freitas, N. Cheung, M.A. Arenas, A.C.d. Campo, J.d. Damborenea, A. García, Microstructure, tensile properties and wear resistance correlations on directionally solidified Al-Sn-(Cu; Si) alloys, in, Elsevier, 2017,

[14] A. Karma, D. Tourret, Atomistic to continuum modeling of solidification microstructures, Current Opinion in Solid State and Materials Science, 20 (2016) 25-36.
[15] W. Kurz, M. Rappaz, R. Trivedi, Progress in modelling solidification microstructures in metals and alloys. Part II: dendrites from 2001 to 2018, Int. Mater. Rev., (2020) 1-47.
[16] H. Nguyen-Thi, G. Reinhart, B. Billia, On the interest of microgravity experimentation for studying convective effects during the directional solidification of metal alloys, Comptes Rendus Mécanique, 345 (2017) 66-77.
[17] N. Bergeon, G. Reinhart, F.L. Mota, N. Mangelinck-Noël, H. Nguyen-Thi, Analysis of gravity effects during binary alloy directional solidification by comparison of microgravity and Earth experiments with in situ observation, The European Physical Journal E, 44 (2021) 98.
[18] D.J. Browne, F. Garcia-Moreno, H. Nguyen-Thi, G. Zimmermann, F. Kargl, R.H. Mathiesen, A. Griesche, O. Minster, Overview of In Situ X-Ray Studies of Light Alloy Solidification in Microgravity, in: K.N. Solanki, D. Orlov, A. Singh, N.R. Neelameggham (Eds.) Magnesium Technology 2017, Springer International Publishing Ag, Cham, 2017, pp. 581-590.
[19] D. Mirković, J. Gröbner, R. Schmid-Fetzer, Solidification paths of multicomponent monotectic aluminum alloys, Acta Mater., 56 (2008) 5214-5222.
[20] W. Zhai, H.M. Liu, B. Wei, Liquid phase separation and monotectic structure evolution of ternary Al62.6Sn28.5Cu8.9 immiscible alloy within ultrasonic field, Materials Letters, 141 (2015) 221-224.
[21] H. Nguyen-Thi, L. Salvo, R.H. Mathiesen, L. Arnberg, B. Billia, M. Suery, G. Reinhart, On the interest of synchrotron X-ray imaging for the study of solidification in metallic alloys, Comptes Rendus Physique, 13 (2012) 237-245.
[22] R.H. Mathiesen, L. Arnberg, H. Nguyen-Thi, B. Billia, In Situ X-Ray Video Microscopy as a Tool in Solidification Science, Jom, 64 (2012) 76-82.
[23] Y. Wang, S. Jia, M. Wei, L. Peng, Y. Wu, X. Liu, Research progress on solidification structure of alloys by synchrotron X-ray radiography: A review, Journal of Magnesium and Alloys, 8 (2020) 396-413.
[24] Y. Zhao, W. He, D. Song, W. Zhang, F. Shen, B. Ma, Y. Jia, Z. Sun, Y. Fu, R. Fernández, In-situ synchrotron X-ray radiography study of primary Fe-rich phases growth in Al-Fe(Cu) alloys, Materials Characterization, 195 (2023) 112539.
[25] P.L. Schaffer, R.H. Mathiesen, L. Arnberg, M.D. Sabatino, A. Snigirev, In situ investigation of spinodal decomposition in hypermonotectic Al–Bi and Al–Bi–Zn alloys, New Journal of Physics, 10 (2008) 053001.
[26] W. Lu, S. Zhang, W. Zhang, G. Kaptay, J. Yu, Y. Fu, J. Li, Direct observation of the segregation driven by bubble evolution and liquid phase separation in Al–10 wt.% Bi immiscible alloy, Scr. Mater., 102 (2015).

[27] W. Lu, S. Zhang, J. Li, Segregation driven by collision and coagulation of minor droplets in Al–Bi immiscible alloys under aerodynamic levitation condition, Materials Letters, 107 (2013) 340-343.
[28] Y. Zhang, Y. Wu, Y. Tang, J. Ma, B. Mao, Y. Xue, H. Xing, J. Zhang, B. Sun, In situ study on the oscillation of mobile droplets and force analysis during the directional solidification of Al-Bi alloy, Journal of Materials Science & Technology, 177 (2024) 1-9.
[29] https://thermocalc.com, Thermo-Calc Software: Computational Materials Engineering
[30] L. Abou-Khalil, J. Wang, G. Salloum-Abou-Jaoude, M. Garrido, X. Li, Z. Ren, G. Reinhart, H. Nguyen-Thi, Y. Fautrelle, Investigation of Thermo-Electro-Magnetic force on equiaxed grain motion during upward directional solidification, Int. J. Therm. Sci., 145 (2019) 106047.
[31] Y. Fautrelle, J. Wang, G. Salloum-Abou-Jaoude, L. Abou-Khalil, G. Reinhart, X. Li, Z. Ren, H. Nguyen-Thi, Thermo-Electric-Magnetic Hydrodynamics in Solidification: In Situ Observations and Theory, JOM Journal of the Minerals, Metals and Materials Society, 70 (2018) 764 - 771.
[32] G. Salloum-Abou-Jaoude, J. Wang, L. Abou-Khalil, G. Reinhart, Z. Ren, N. Mangelinck-Noel, X. Li, Y. Fautrelle, H. Nguyen-Thi, Motion of equiaxed grains during directional solidification under static magnetic field, Journal of Crystal Growth, 417 (2015) 25-30.
[33] U. Hecht, L. Gránásy, T. Pusztai, B. Böttger, M. Apel, V. Witusiewicz, L. Ratke, J. De Wilde, L. Froyen, D. Camel, B. Drevet, G. Faivre, S.G. Fries, B. Legendre, S. Rex, Multiphase solidification in multicomponent alloys, Materials Science and Engineering: R: Reports, 46 (2004) 1-49.
[34] W. Boettinger, U. Kattner, K.-W. Moon, J. Perepezko, NIST Recommended Practice Guide: DTA and Heat-Flux DSC Measurements of Alloy Melting and Freezing, in, Elsevier, Kidlington, -1, 2006,
[35] S. Curiotto, L. Battezzati, E. Johnson, N. Pryds, Thermodynamics and mechanism of demixing in undercooled Cu-Co-Ni alloys, Acta Mater., 55 (2007) 6642-6650.
[36] S. Akamatsu, H. Nguyen-Thi, In situ observation of solidification patterns in diffusive conditions, Acta Mater., 108 (2016) 325-346.
[37] H. Soltani, G. Reinhart, M.C. Benoudia, F. Ngomesse, M. Zahzouh, H. Nguyen-Thi, Equiaxed grain structure formation during directional solidification of a refined Al-20wt.%Cu alloy: In situ analysis of temperature gradient effects, Journal of Crystal Growth, 587 (2022) 126645.
[38] H. Soltani, G. Reinhart, M.C. Benoudia, F. Ngomesse, M. Zahzouh, H. Nguyen-Thi, Impact of growth velocity on grain structure formation during directional solidification of a refined Al-20 wt.%Cu alloy, Journal of Crystal Growth, 548 (2020) 125819.
[39] H. Soltani, G. Reinhart, M.C. Benoudia, M. Zahzouh, H. Nguyen-Thi, Impact of gravity-related phenomena on the grain structure formation: comparative study between horizontal and vertical solidification of a refined Al-20wt.%Cu alloy, IOP Conference Series: Materials Science and Engineering, 529 (2019) 012019.

[40] F. Ngomesse, G. Reinhart, H. Soltani, G. Zimmermann, D.J. Browne, W. Sillekens, H. Nguyen-Thi, In situ investigation of the Columnar-to-Equiaxed Transition during directional solidification of Al–20 wt.%Cu alloys on Earth and in microgravity, Acta Mater., 221 (2021) 117401.

[41] H. Nguyen-Thi, G. Reinhart, G.S. Abou Jaoude, R.H. Mathiesen, G. Zimmermann, Y. Houltz, D. Voss, A. Verga, D.J. Browne, A.G. Murphy, XRMON-GF: A novel facility for solidification of metallic alloys with in situ and time-resolved X-ray radiographic characterization in microgravity conditions, Journal of Crystal Growth, 374 (2013) 23-30.

[42] M.G.C. Xavier, R.A.V. Reyes, L.F. Gomes, J.E. Spinelli, N. Mangelinck-Noël, H. Nguyen-Thi, G. Reinhart, Combined growth of α-Al and Bi in a Al-Bi-Cu monotectic alloy analyzed by in situ X-ray radiography, Journal of Crystal Growth, 536 (2020) 125592.

[43] G. Reinhart, F. Ngomesse, F. Bertelli, P. Benigni, A. Campos, H. Nguyen-Thi, Investigation of Al-20Sn-10Cu alloy directional solidification by laboratory X-radiography, IOP Conference Series: Materials Science and Engineering, 1274 (2023) 012054.

[44] C.A. Schneider, W.S. Rasband, K.W. Eliceiri, NIH Image to ImageJ: 25 years of image analysis, Nature Methods, 9 (2012) 671-675.

[45] H. Nguyen-Thi, G. Reinhart, A. Buffet, T. Schenk, N. Mangelinck, H. Jung, N. Bergeon, B. Billia, H. Härtwig, J. Baruchel, In situ and Real-time analysis of TGZM phenomena by synchrotron X-ray radiography, J. of Crystal Growth, 310 (2008) 2906-2914.

[46] G. Reinhart, D. Grange, L. Abou-Khalil, N. Mangelinck-Noël, N.T. Niane, V. Maguin, G. Guillemot, C.A. Gandin, H. Nguyen-Thi, Impact of solute flow during directional solidification of a Ni-based alloy: In-situ and real-time X-radiography, Acta Mater., 194 (2020) 68-79.

[47] P.L. Schaffer, R.H. Mathiesen, L. Arnberg, L-2 droplet interaction with alpha-Al during solidification of hypermonotectic Al-8 wt.% Bi alloys, Acta Mater., 57 (2009) 2887-2895.

[48] W. Kurz, D.J. Fisher, M. Rappaz, Fundamentals of Solidification, Trans Tech Publications ltd, , 2023.

[49] P. Chao, G.R. Lindemann, A.H. Hunter, A.J. Shahani, Pseudo-4D view of the growth and form of locked eutectic colonies, Acta Mater., 240 (2022) 118335.

[50] W.U. Mirihanage, K.V. Falch, I. Snigireva, A. Snigirev, Y.J. Li, L. Arnberg, R.H. Mathiesen, Retrieval of three-dimensional spatial information from fast in situ two-dimensional synchrotron radiography of solidification microstructure evolution, Acta Mater., 81 (2014) 241-247.

[51] N. Wang, Y. Tang, Y. Wu, Y. Zhang, Y. Dai, J. Zhang, R. Zhang, Y. Xu, B. Sun, Dynamic evolution of microstructure morphology in thin-sample solidification: Deep learning assisted synchrotron X-ray radiography, Materials Characterization, 181 (2021) 111451.